Plasma Chemistry and Plasma Processing (2024) 44:1575–1594
https://doi.org/10.1007/s11090-024-10484-6

ORIGINAL PAPER

Modeling Study of Chemical Kinetics and Vibrational Excitation in a Volumetric DBD in Humid Air at Atmospheric Pressure

Giacomo Pierotti[1] · **Arturo Popoli**[1] · **Carlos Daniel Pintassilgo**[2,3] · **Andrea Cristofolini**[1]

Received: 19 March 2024 / Accepted: 1 June 2024 / Published online: 20 June 2024

Abstract
A zero-dimensionl model is developed to study the chemical kinetics of a volumetric dielectric barrier discharge (DBD) reactor operating with humid air at atmospheric pressure. This work focuses on the relation between molecular vibrational excitation, the plasma reactor input power and the number densities of several species that are known to play an important role in biomedical applications (e.g. O_3, NO, NO_2, ...). A preliminary study is carried out to observe the influence of water molecules on the electron energy distribution function for different values of water concentration and reduced electric field. A simplified approach is then adopted to quantify the contribution of vibrationally-excited O_2 molecules to NO formation. The results obtained using our detailed model suggest that for the physical conditions considered in this work O_2 vibrational kinetics can be neglected without compromising the overall accuracy of the simulation. Finally, a reaction set is coupled with an equivalent circuit model to simulate the E-I characteristic of a typical DBD reactor. Different simulations were carried out considering different values of the average plasma input power densities. A particular focus was given to the influence of the Zeldovich mechanism on O_3 and NO_X production performing simulations where this reaction is not considered. The obtained results are shown and the role of vibrationally excited N_2 molecules is discussed. The simulation results indicate also that N_2 vibrational excitation, and more precisely the Zeldovich mechanism, has a larger effect on O_3 and NO_X production at intermediate input power levels.

Keywords Vibrational excitation · Dielectric barrier discharge · Air plasma · Equivalent circuit · Plasma Modeling

✉ Giacomo Pierotti
giacomo.pierotti2@unibo.it

[1] Department of Electrical, Electronic and Information Engineering "Guglielmo Marconi", University of Bologna, Viale Risorgimento 2, 40134 Bologna, Italy

[2] Departamento de Engenharia Física, Faculdade de Engenharia, Universidade do Porto, R. Dr Roberto Frias, 4200-465 Porto, Portugal

[3] Instituto de Plasmas e Fusão Nuclear, Instituto Superior Técnico, Universidade de Lisboa, 1049-001 Lisboa, Portugal

Introduction

Non-thermal plasmas play an important role in many different applications, ranging from biomedicine, to combustion and aerospace. In particular, reactive oxygen and nitrogen species (RONS) generated in a cold plasma are known to play a central role in volume and surface sanitation, cancer treatments, wound healing, plasma assisted agriculture and food processing [1–3]. A lot of effort has been put in investigating the main chemical species and reaction mechanisms that are important in the above mentioned applications. In [4], Shimizu et al. showed a correlation between the inactivation of Escherichia coli and the time-averaged O_3 number density produced by a surface DBD. In [5] the antimicrobial properties of NO_X compounds are proved through experimental measurements. NO also plays an important role in wound healing as reported in different studies [1, 6]. Seri et al. proved the efficacy of sterilization by means of an indirect treatments of medical disposable devices with RONS generated by an atmospheric pressure plasma jet [7]. Various RONS (e.g. NO, OH, $O(^3P)$, ...) that can be generated using a cold plasma device are signaling species [8] that may enhance seed germination and fasten growth of a large set of plants [9]. One of the most accessible ways to control the production of RONS is by means of dielectric barrier discharge reactors operating at atmospheric pressure. These are commonly employed in volumetric and surface configurations. The kinetic mechanisms behind RONS production in such devices are very complex and strongly interconnected with each other. For example, in different studies on surface DBDs [4, 10] the importance of the N_2 vibrational distribution function (VDF) for the formation of NO (with the consequent O_3 depletion due to the reaction $NO + O_3 \longrightarrow NO_2 + O_2$) is reported. Conversely, to date, the role of vibrational excitation of O_2 for RONS production was not investigated in detail, at least for DBD devices. To represent the vibrational kinetics of both N_2 and O_2, a large set of reactions and species is needed. In addition to that, to correctly describe the chemical processes involved in RONS production, other different types of reactions are needed, such as electron collisions, ionic charge-exchange collisions and heavy-species collisions. This makes 2-D and even 1-D models rather unsuited to study phenomena that span over hundreds of milliseconds, the more so when convective and diffusive fluxes are important too [11]. In this spirit, due to the complexity of the phenomena taking place in DBD reactors, global modeling approaches represent useful tools to better understand and optimize the production of reactive species.

In this work we use a global kinetic model to perform a computational study on the plasma kinetics of a volumetric DBD reactor operating with humid air at atmospheric pressure. The focus of the study is on vibrational kinetics and the evolution of reactive species relevant to biological applications. Ultimately, our results suggest that – for the physical conditions considered in this work – O_2 vibrational kinetics can be neglected without compromising the overall accuracy of the simulation. In Sect. 2 the computational kinetic model is described, while in Sect. 3 a preliminary study is carried out to assess the influence of humidity on the electron energy distribution function (EEDF) and the role of oxygen vibrational excitation in reactive species production. In Sect. 4 we describe the derivation and computer implementation of the equivalent electric circuit model proposed by Colonna et al. in [12]. Finally, in Sect. 4.2 the results on the N_2 VDF and reactive species kinetics are reported and discussed.

Kinetic Model

General Description

In this work, two different reaction sets have been used to model the discharge dynamics. The first one, used in the preliminary study described in Sect. 3, includes 65 species (reported in Table 1) and nearly 9000 reaction mechanisms. These include electron impact reactions (excitation, ionization, attachment, dissociation and recombination), ionic charge exchange, vibrational excitation of N_2 and O_2 molecules and heavy neutral species collisions. The reaction coefficient for heavy species collisions and charge exchange collisions have been taken from [13], while processes involving vibrationally excited oxygen and nitrogen molecules were taken from [14] and [15]. 60 vibrational levels have been considered for N_2 molecules and 42 for O_2. Reactions describing electronically-excited states of N_2 and NO are taken from [16] and [17] respectively. The second reaction set, adopted for the calculations described in Sect. 4.2 is composed by nearly 5000 reactions and does not account for the vibrational kinetics of oxygen molecules, for the reasons that will be given in Sec. 3. The two reaction sets will be referred hereon as *full* and *reduced*, respectively.

Regardless of the considered kinetic scheme, the number density evolution of each considered species is obtained solving the volume-averaged particle balance equation:

$$\frac{\mathrm{d}n_i}{\mathrm{d}t} = \sum_j C_{ij} R_j^i, \tag{1}$$

where n_i is the number density of the $i-$th species, R_j^i is the rate of the $j-$th reaction the includes the $i-$th species, C_{ij} is the net stoichiometric coefficient fer the species i in the $j-$th reaction. R_j^i can be expressed as:

$$R_j^i = k^j \prod_l n_l^r, \tag{2}$$

where k_j is the rate coefficient for the considered reaction, n_l is the number density of each species involved in the reaction, l and r are the forward and backward stoichiometric coefficients, respectively. All the rate coefficients for the electron impact reactions have been calculated before the simulation for different values of the reduced electric field solving the electron Boltzmann equation (EBE) using the LoKI-B tool [18, 19]. This was performed considering a ternary mixture of N_2 (78%), O_2 (19%) and H_2O (3%). The cross sections

Table 1 Species considered in the simulations. Each vibrationally-excited level is treated like a single species. $O_2(Sum)$ represents the sum of the states $O_2(A^3\Sigma_u^+)$, $O_2(C^3\Delta_u)$ and $O_2(c^1\Sigma_u^-)$

$N_2(X, 0 \leq v \leq 59), N_2(A^3\Sigma_u^+), N_2(B^3\Pi_g), N_2(C^3\Pi_u), N_2(a'\Sigma_u^-), N_2(w^1\Delta_u), N_2(a^1\Pi_g), N_2^+, N_2^+(B^2\Sigma_u^+)$
$N(^4S), N(^2D), N(^2P), N^+, N_4^+, N_3^+$
$O_2(X, 0 \leq v \leq 41), O_2(a^1\Delta_g), O_2(b^1\Sigma_g^+), O_2(Sum), O_2^+, O_2^-$
$O(^3P), O(^1D), O^+, O^-, O_3, O_3(exc), O_3^-, O_4^-, O_4^+$
$NO, NO(A^2\Sigma^+), NO(B^2\Pi), NO^+, NO^-, NO_2, NO_2^+, NO_2^-, NO_2(A)$
$NO_3, NO_3^-, N_2O, N_2O^+, N_2O^-N_2O_3, N_2O_4, N_2O_5$
$H_2O, H_2O^+, H_3O^+, H, H^+, H^-, OH, OH^+, OH^-, H_2, H_2^+, H_3^+, HO_2, H_2O_2$
HNO, HNO_2, HNO_3, e

for electron impact reactions with H_2O molecules were taken from [20], while ones of all the other processes have been retrieved from the online database LXCat [21–23]. Convective and diffusive fluxes have not been considered since all the simulations have been conducted considering static conditions.

Vibrational Kinetics

The largest part of the *full* kinetic model consists in reactions involving vibrationally-excited states of N_2 and O_2 that will be described in more details in this section. As already mentioned, we have considered 60 vibrational levels for nitrogen molecules and 42 for the oxygen ones. In both cases the anharmonic oscillator approximation was used to describe the energetic levels of the states. Collisions with electrons (e-V collisions) are considered for both molecular species in the form:

$$e + N_2(v) \longleftrightarrow e + N_2(v'), \tag{3}$$

$$e + O_2(v) \longleftrightarrow e + O_2(v'). \tag{4}$$

All the reaction rates for e-V collisions for O_2 have been obtained from cross sections of the IST database [24] together with the ones of rates between electrons and $N_2(v = 0)$ [25]. For higher nitrogen vibrational levels, the scaling law proposed in [15] has been used. Collisions between vibrationally-excited molecules (V-V) have been taken in to account through the following reactions:

$$N_2(v) + N_2(w) \longleftrightarrow N_2(v + 1) + N_2(w - 1) \tag{5}$$

$$O_2(v) + O_2(w) \longleftrightarrow O_2(v + 1) + O_2(w - 1). \tag{6}$$

The associated rate constants have been taken from [14]. Vibrational relaxation through V-T collisions is also considered in the model and is represented by the reactions:

$$N_2(v) + M \longleftrightarrow N_2(v - n) + M \tag{7}$$

$$O_2(v) + M \longleftrightarrow O_2(v - n) + M, \tag{8}$$

where M represents four different species: N_2, (O_2), $O(^3P)$ and $N(^4S)$. For N_2, O_2 and $O(^3P)$ only single-quanta relaxations are considered (i.e. $n = 1$). Conversely, for $M = N(^4S)$ multi-quanta transitions are not negligible and so n spans from 1 to 5. The corresponding rate constants have been taken from [14] and [26]. Finally, both Zeldovich mechanisms have been considered:

$$N_2(v > 12) + O(^3P) \longrightarrow NO + N(^4S) \tag{9}$$

$$O_2(v > 1) + N(^4S) \longrightarrow NO + O(^3P) \tag{10}$$

Reaction (9) is considered in many different studies, albeit with different rate constant, i.e. $k_{(9)} = 10^{-17}\mathrm{m}^3/\mathrm{s}$ in, e.g., [16] and $k_{(9)} = 10^{-19}\mathrm{m}^3/\mathrm{s}$ in, e.g., [27]. The latter has been used in this study. Concerning reaction (10), a detailed set of rate constants depending of the actual considered vibrational level is reported in [28]. Nevertheless we adopted the constant value $k_{(10)} = 3 \times 10^{-18}\mathrm{m}^3/\mathrm{s}$ already used in [29] for the sake of simplicity.

Influence of Humidity on EEDF and Role of Vibrational Excitation of O_2 in Chemical Kinetics

Role of Humidity on the EEDF

To asses the influence of water content on the EEDF behavior, the LoKI-B code [18, 19] was used to solve the Boltzmann equation for different values of the reduced electric field *E/N* (10Td to 150Td) assuming a gas temperature $T = 300$K. These values have been chosen as representative of discharge conditions of a typical volumetric DBD reactor powered by a sinusoidal voltage waveform at atmospheric pressure. For each reduced field value, two different gas mixtures were tested. The first, corresponding to dry air, does not include any water molecules, while the other one has a 3% water concentration. The latter value corresponds to $\approx 100\%$ of relative humidity (RH) at atmospheric pressure with a gas temperature of $T = 300$K. As shown in Fig. 1, while the RH changes the EEDF for $E/N = 10$Td, water content does not seem to significantly influence the EEDF shape for $E/N = 20$Td. This is also valid for higher reduced field values, that have not been reported in Fig. 1. This is consistent with the results of other authors that are available in literature [30]. The obtained results show that including the cross sections for electron impact reactions with water molecules is not mandatory to correctly solve the EBE for reduced field levels relevant for the study of DBDs in atmospheric pressure air.

Influence of O_2 Vibrational Excitation

The *full* set described in Sect. 2 has been used to perform several simulations to evaluate the influence of O_2 vibrational excitation on the discharge kinetics. In particular, the effects of reaction (10) $O_2(v > 1) + N(^4S) \longrightarrow NO + O(^3P)$ on $NO, O(^3P)$ and $N(^4S)$ have been investigated. The discharge evolution is followed by alternating discharge and afterglow phases. The discharge phase is modeled by fixing the reduced field *E/N* and the electron number density n_e over a time interval t_{disch}. A discharge phase is followed by an afterglow phase over a time-span t_{aft}, in which both n_e and *E/N* are set to 0. The two phases

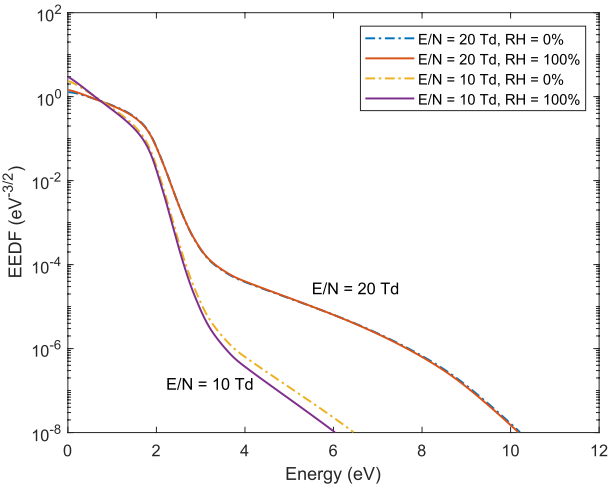

Fig. 1 EEDF at 10Td and 20Td for 0% (dash-dotted line) and 100% (continuous line) of relative humidity (RH). For $E/N \geq 20$Td the influence of humidity on the EEDF is negligible

Table 2 Reaction rates in m^{-3}/s and relative contribution of reaction (10) $O_2(v > 1) + N(^4S) \longrightarrow NO + O(^3P)$ on NO and $O(^3P)$ production and on $N(^4S)$ destruction for the two considered values of t_{aft}

	First afterglow phase		Last afterglow phase	
	$t_{aft} = 10^{-6}$s	$t_{aft} = 10^{-5}$s	$t_{aft} = 10^{-6}$s	$t_{aft} = 10^{-5}$s
Reaction rate of (10)	1.00×10^{25}	6.70×10^{23}	1.28×10^{25}	2.20×10^{23}
Contribution to $N(^4S)$	6.5%	3.5%	2.2%	1.0%
Contribution to $O(^3P)$	4.7%	0.35%	0.29%	0.2%
Contribution to NO	5.4%	1.5%	0.38%	0.1%

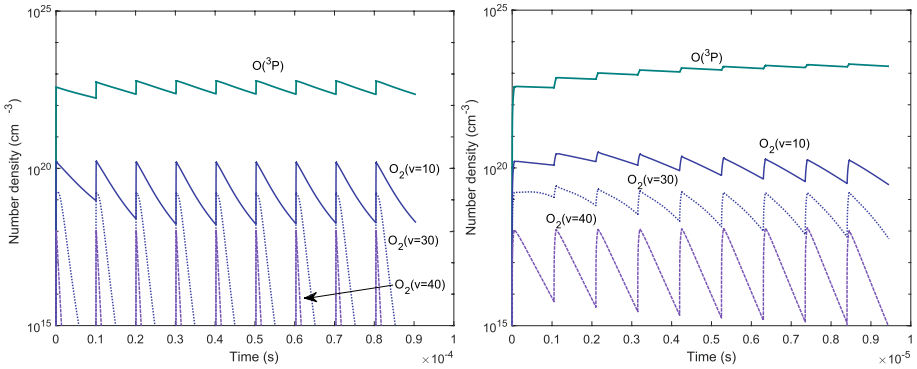

(a) $t_{aft} = 10^{-5}$ s (b) $t_{aft} = 10^{-6}$ s

Figure 2: $O(^3P)$, O_2(v=10), O_2(v=30) and O_2(v=40) for two afterglow durations.

Fig. 2 $O(^3P)$, $O_2(v = 10)$, $O_2(v = 30)$ and $O_2(v = 40)$ for two afterglow durations

are alternated until the the vibrational distribution function (VDF) of O_2 reaches periodic regime or starts to be substantially depopulated. Two different simulations were carried out, using different values for t_{aft}, i.e. $t_{aft} = 10^{-5}$s and $t_{aft} = 10^{-6}$s. The other parameters, chosen to represents a typical behavior of a volumetric DBD discharge based on various published papers [31–33], are $E/N = 150$Td, $n_e = 10^{19}m^{-3}$ and $t_{disch} = 50$ns. The gas temperature has been considered constant at 300K. The relative contribution of reaction (10) in NO(X) and $O(^3P)$ formation and in $N(^4S)$ destruction is evaluated at the end of the first and the last afterglow phases. The results are reported in Table 2 for both the considered values of t_{aft}.

The results in Table 2 show that reaction (10) does not play a significant role in any of the three considered species generation/loss. Moreover, its relative contribution decreases over time. This is mainly due to the increase of atomic oxygen (reported below in Fig. 2) that activates the V-T relaxation:

$$O_2(v) + O(^3P) \longrightarrow O_2(v-1) + O(^3P), \tag{11}$$

that is very effective in relaxing O_2 vibrational states. The importance of reaction (11) in the relaxation of the first levels of O_2 VDF has been proved also at intermediate and low pressures (i.e. from mTorr to Torr) in [34] and [35]. Figures 2a and b report the computed

behavior of oxygen atoms and of three vibrational states of O_2 (i.e. $v = 10$, $v = 30$ and $v = 40$). In Fig. 2b is clearly shown that, for all the considered vibrational levels, the corresponding number densities decrease more rapidly at the beginning of each afterglow phase, when the number density of $O(^3P)$ is higher. This effect can also be seen in Fig. 2a, albeit only for the $O_2(v = 10)$ state since the number density of the other two states falls below $10^{15}m^{-3}$ after the end of the first afterglow. The most interesting difference yielded by the larger afterglow time in Fig. 2a is that a periodic regime of the number densities is reached earlier.

To better understand the vibrational kinetics in the considered conditions, O_2 and N_2 vibrational temperatures have been calculated for both simulations according to the equation [36]:

$$T_{vib} = \frac{E_{0,1}}{\ln\left(\frac{n_{v=0}}{n_{v=1}}\right)}, \tag{12}$$

where $E_{0,1}$ is the energy difference between the ground state and the first vibrationally excited level, i.e. 0.193eV for O_2 and 0.289eV for N_2, $n_{v=0}$ and $n_{v=1}$ are the corresponding number densities. The results are reported in Fig. 3a and b.

The results show that the vibrational temperature of O_2 remains between 300 and 400K for both considered values of t_{aft} and reaches periodic state in less than 6 pulses. On the other hand, the vibrational temperature of N_2 is still raising at the end of both considered values of t_{aft}. This effect shows that N_2 VDF evolves slower than the one of O_2. Weak vibrational excitation of O_2 molecules in atmospheric pressure air has been measured in [37], supporting our numerical result. Equation (12) accounts only for the first two vibrational levels. However, the other levels can also be important for the discharge kinetics. To provide more insight on the vibrational excitation, the VDFs at the beginning and at the end of each afterglow phase and the vibrational temperature calculated considering all the vibrational levels are reported in Figs. 4. The O_2 VDF shape, characterized by a large plateau in correspondence of the intermediate levels, is similar to the ones found in [34] and [35] for lower pressure levels. The proposed mechanisms that lead to the plateau formation are the three body recombination of $O(^3P)$ atoms and the multi-quanta e-V excitation at

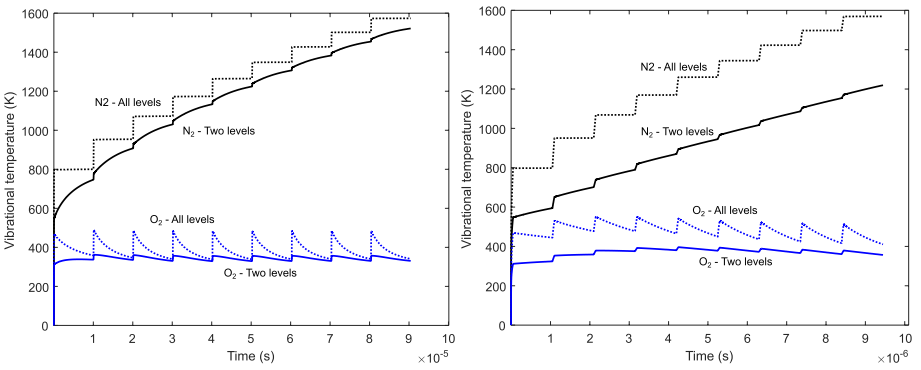

(a) $t_{\text{aft}} = 10^{-5}$ s (b) $t_{\text{aft}} = 10^{-6}$ s

Fig. 3 *Two-level* vibrational temperatures (via Eq. (12)) of O_2 and N_2 considering two different afterglow times

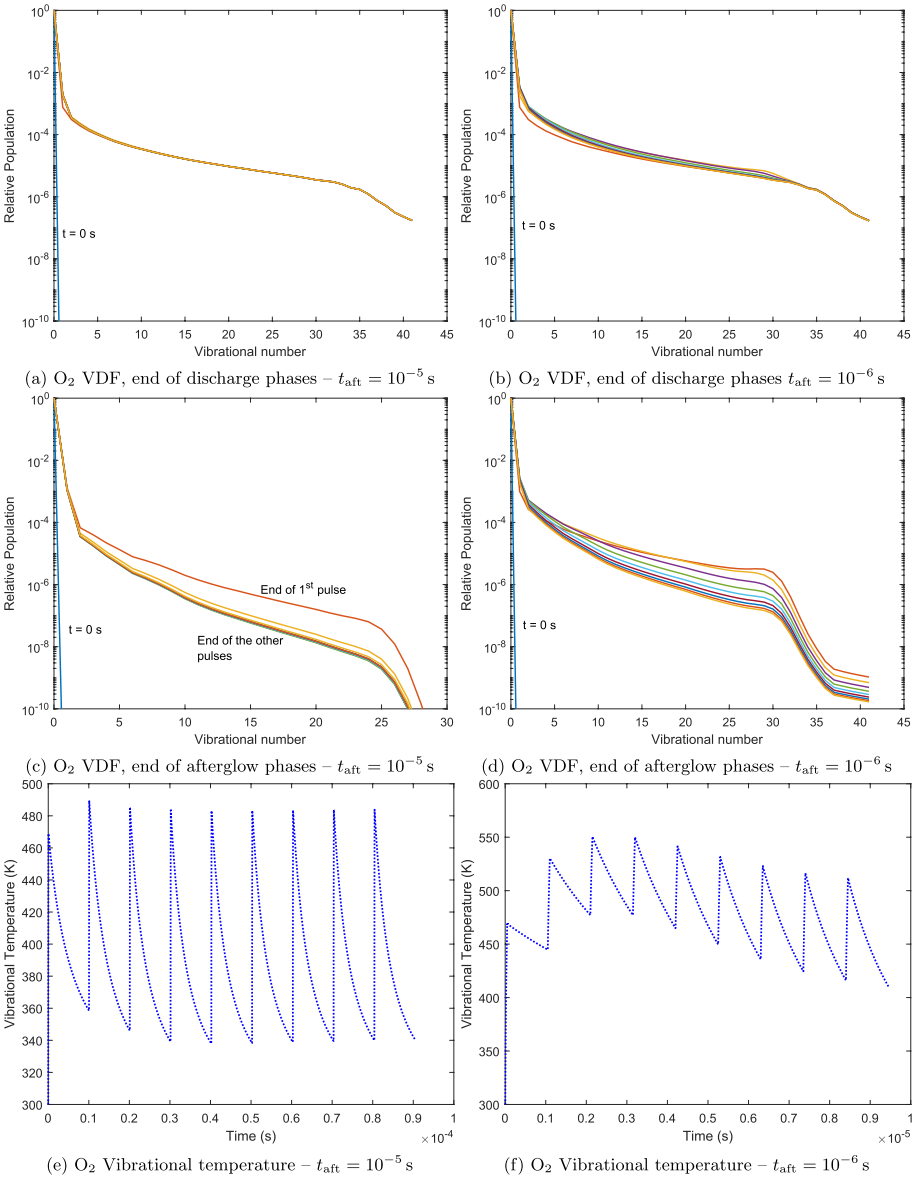

(a) O_2 VDF, end of discharge phases – $t_{\mathrm{aft}} = 10^{-5}$ s

(b) O_2 VDF, end of discharge phases $t_{\mathrm{aft}} = 10^{-6}$ s

(c) O_2 VDF, end of afterglow phases – $t_{\mathrm{aft}} = 10^{-5}$ s

(d) O_2 VDF, end of afterglow phases – $t_{\mathrm{aft}} = 10^{-6}$ s

(e) O_2 Vibrational temperature – $t_{\mathrm{aft}} = 10^{-5}$ s

(f) O_2 Vibrational temperature – $t_{\mathrm{aft}} = 10^{-6}$ s

Fig. 4 O_2 VDF at the end of each afterglow and discharge phases and *all-level* vibrational temperature calculated for both the considered afterglow times. Each line in Figs. 4a, b, c and d corresponds to a different pulse

low and intermediate pressure, respectively. Both the mechanisms are included in the reaction set adopted in this study. The temperature is obtained by solving the following nonlinear equation [38]:

$$\frac{\sum E_v n_v}{\sum n_v} = \frac{\sum E_v \exp\left(-\frac{E_v}{k_B T_{vib,all}}\right)}{\sum \exp\left(-\frac{E_v}{k_B T_{vib,all}}\right)}, \tag{13}$$

where E_v is the energy associated with the $v-$th level of the considered vibrationally excited molecule, n_v is the corresponding number density and k_B is the Boltzmann constant. The obtained vibrational temperature is the one of a Maxwellian distribution with the same mean energy of the strongly non-equilibrium vibrational distribution obtained by the simulations [38].

In Fig. 4a and b it is clearly shown that the VDF at the end of each discharge phase remains nearly the same, while its variation is more evident at the end of each afterglow phase as shown in Fig. 4c and d. These effects can also be deduced observing the behavior of the vibrational temperature in Figs. 4e and f. In fact, the *all-level* vibrational temperature changes less than 10K for $t_{\text{aft}} = 10^{-5}$s and less than 40K for $t_{\text{aft}} = 10^{-6}$s at the end of each discharge phase. Similar considerations can be done for the *all-level* vibrational temperature value at the end of each afterglow phases. $T_{v,all}$ value at the end of each afterglow phases stays between 360 and 340K for $t_{\text{aft}} = 10^{-5}s$ and between 420 and 480K for $t_{\text{aft}} = 10^{-6}$s.

These results show that, even considering all the vibrationally excited levels of O_2, the vibrational temperature remains between 300 and 600K for both the considered simulations and does not reach high enough values to influence the global kinetics of the DBD discharge. From this parametric analysis we can conclude that, for the conditions considered in this study, it is possible to neglect the time-evolution of the vibrationally excited oxygen species without effectively influencing the discharge kinetics. Moreover, O_2(v) influence becomes lower for longer afterglow times. We highlight that the description of the detailed vibrational kinetics of O_2 requires thousands of reactions and that not including these mechanisms in the computational model can effectively reduce the required computational effort. For this reason, oxygen vibrational kinetics will not be included in the chemistry calculations in the next sections. Nevertheless, the excitation from $O_2(v = 0)$ to $O_2(v = 1, 2, 3, 4)$ will still be considered in the EEDF calculation.

Influence of N2 Vibrational Excitation on Reactive Species Production

Equivalent Circuit and ODE

As already mentioned, we implemented an equivalent circuit model to represent the typical E-I characteristic of a volumetric DBD reactor. The model was originally proposed in [12] to study vibrational excitation in an H_2 discharge. The equivalent circuit is shown in Fig. 5. V_0 represents the external voltage source, R_0 is an external resistor, R_p is a variable resistor that represents the plasma resistive effects and C is the capacitance of the dielectric layers of the DBD reactor. In all the performed simulations we will assume $R_0 = 0\Omega$ since the external resistance is usually not needed in a typical volumetric DBD because the current is limited by the dielectric layers.

The Kirchoff's voltage law for the considered circuit can be written as:

$$V_0 - v_p - v_C = 0, \tag{14}$$

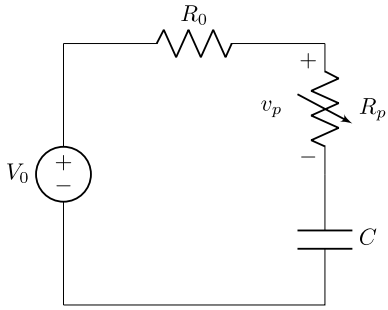

Fig. 5 DBD equivalent electric circuit

where v_p is the voltage drop on R_p and v_C the one on the capacitor. Dividing by the distance d between the electrodes one can obtain:

$$E_0 - E_p - \frac{v_C}{d} = 0, \tag{15}$$

where $E_0 = V_0/d$ and $E_p = v_p/d$. The current i of the circuit can be written in two different ways:

$$i = qn_e\mu_e E_p S_{\text{eff}}, \tag{16}$$

and

$$i = C\frac{dv_C}{dt}. \tag{17}$$

In Eq. (16) q is the elementary charge, n_e is the electron number density, μ_e is the electron mobility and S_{eff} is the effective discharge surface. Note that in a DBD at atmospheric pressure working with a sinusoidal voltage, a filamentary regime is often present. For this reason, S_{eff} is usually assumed to be some percent of the total surface of the dielectric layers [31, 32]. Combining Eqs. (17), (16) and (15) one obtains:

$$\frac{\mathrm{d}E_p}{\mathrm{d}t} = \frac{\mathrm{d}E_0}{\mathrm{d}t} - \frac{1}{d}\frac{\mu q n_e E_p S_{\text{eff}}}{C}. \tag{18}$$

The quantities C, S_{eff} and d can be used to define $C_0 = \frac{Cd}{S_{\text{eff}}}$. The latter, along with the frequency f of the voltage source, is the parameter that can be modified to perform simulations corresponding to the different input power levels. Equation (18) can be solved together with the set of Eqs. (1) for every species considered in the model, obtaining the system of ordinary differential equations (ODEs):

$$\begin{cases} \frac{\mathrm{d}n_1}{\mathrm{d}t} = \sum_j \left[(a^R_{1j} - a^L_{1j})k_j \prod_l n_l\right] \\ \quad\vdots \\ \frac{\mathrm{d}n_n}{\mathrm{d}t} = \sum_j \left[(a^R_{nj} - a^L_{nj})k_j \prod_l n_l\right] \\ \frac{\mathrm{d}E_p}{\mathrm{d}t} = \frac{\mathrm{d}E_0}{\mathrm{d}t} - \frac{1}{d}\frac{\mu q n_e E_p S_{\text{eff}}}{C} \end{cases} \tag{19}$$

Where a_{ij}^R and a_{ij}^L are the right-hand side and left-hand side stoichiometric coefficients of species i in the reaction j. The system is solved in MATLAB using the |ode15s| function for stiff ODE systems [39].

Simulation Results

Three different simulations have been carried out considering different levels of the average electrical input power density. The simulations corresponding to the three levels will be indicated as P_1, P_2 and P_3 hereon. The three levels are obtained by changing the values of C_0 in the equivalent circuit and the frequency f of $V_0(t)$. The discharge gap $d = 1$mm and the amplitude of the applied voltage $V_{0,M} = 10$kV are the same in all the simulations. $P_1 = 2.7 \times 10^6 \mathrm{W/m^3}$ – the highest input power density that we considered in this study – corresponds to $f_1 = 10$kHz and $C_0 = 10^4 \epsilon_0 \mathrm{F/m}$. These values are the same as in [12]. The parameters yielding the other two power density levels $P_2 = 1.35 \times 10^5 \mathrm{W/m^3}$ and $P_3 = 1.45 \times 10^3 \mathrm{W/m^3}$ are $f = 10\mathrm{kHz}, C_0 = 500\epsilon_0 \frac{F}{m}$ and $f = 5\mathrm{kHz}, C_0 = 10\epsilon_0 \frac{F}{m}$, respectively. The gas temperature was fixed at 300K. The obtained results are shown in Fig. 6. In the following sections we analyze the behavior of several key species.

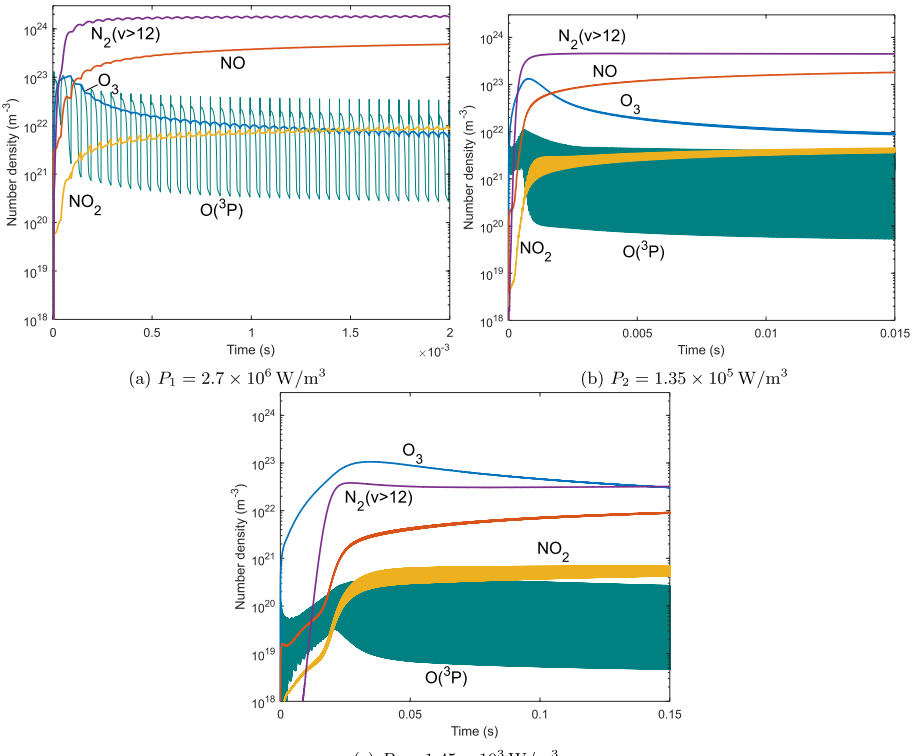

(a) $P_1 = 2.7 \times 10^6\ \mathrm{W/m^3}$ (b) $P_2 = 1.35 \times 10^5\ \mathrm{W/m^3}$

(c) $P_3 = 1.45 \times 10^3\ \mathrm{W/m^3}$

Fig. 6 Behavior of O_3, NO, NO_2, $O(^3P)$ and $N_2(v > 12)$ number densities for the considered input power levels

O_3 and NO

As may be observed in Fig. 6a, b and c, different input power levels change significantly both the dynamics and the final concentration levels of O_3, NO_X and $N_2(v)$. In all three simulations, the ozone number density increases rapidly as soon as the discharge is turned on due to reactions:

$$e + O_2 \longrightarrow e + O(^3P) + O(^3P), \tag{20}$$

$$O_2 + O(^3P) + M \longrightarrow O_3 + M. \tag{21}$$

Atomic oxygen is created by reaction (20) trough dissociation of O_2. Ozone is subsequently generated by reaction (21), in which the species M denotes N_2 and O_2. At the beginning of the discharge, only the lower levels of the nitrogen VDF are populated due to the fast e-V collisions in reaction (22):

$$e + N_2(v = n) \longrightarrow e + N_2(v = n + 1). \tag{22}$$

Consequently, the Zeldovich mechanism $N_2(v > 12) + O(^3P) \longrightarrow NO + N(^4S)$, which involves only vibrational levels with $v > 12$, does not influence the discharge kinetics at this stage.

The V-V collisions in Eq. (56) start to populate higher levels of the VDF only later on, causing the observed NO number density increase. The higher availability of NO enhances O_3 losses through reaction (23):

$$NO + O_3 \longrightarrow NO_2 + O_2. \tag{23}$$

O_3 and NO_X dynamics are strongly influenced by the input power. In fact, as shown in Figs. 6a, b and c, the discharge chemistry is substantially different in the three considered simulations. In particular, for P_3 the discharge kinetics dominated by O_3 and the NO number density is nearly two orders of magnitude lower with respect to the O_3 during the whole simulation. Increasing the power, NO_X compounds start to become preponderant.

For the intermediate power level P_2, the O_3 number density is higher with respect to NO only for the first $\sim$ 1.5ms. At the end of the P_2 simulation, i.e. after 15ms, the NO number density is larger with respect to the one of O_3 but the NO_2 concentration remains the lowest among the three considered species.

Finally, for the highest power density level, P_1, the discharge kinetics is completely NO_X dominated. Starting from the beginning of the simulation, the O_3 number density becomes smaller than the one of NO after $\sim$ 0.18ms. At the end of the simulation even the NO_2 density is larger than O_3. This behaviour is caused by the well known ozone poisoning mechanism, experimentally investigated in [40]. The ozone poisoning mechanism is related to the presence of NO_X compounds in the plasma region. These chemical species act in two different ways against ozone formation: they directly quench ozone ($NO + O_3 \longrightarrow NO_2 + O_2$, $NO_2 + O_3 \longrightarrow NO_3 + O_2$) and react with oxygen atoms ($NO + O + M \longrightarrow NO_2 + M$, $NO_2 + O + M \longrightarrow NO_3 + M$) lowering the reaction rate of the main O_3 creation mechanism $O + O_2 + M \longrightarrow O_3 + M$. Due to these reactions, the ozone concentration decreases as soon as the NO_X number density increases. The process is faster for higher power densities. For this reason, O_3 cannot be formed at all in NO_X rich environments. The behavior of NO_2 will be discussed further below in Sect. 4.2. As shown in the Fig. 6, ozone depletion begins as soon as the NO number density starts to increase due to the already mentioned

reaction (23). The three figures highlight that the O_3 quenching process is faster for larger input power levels of the DBD reactor. This is due to the fact that the discharge voltage (v_p in Fig. 5) does not change significantly with the input power of DBD reactors [41]. Rather, increasing the power density leads to larger average values of the electron number density n_e. This can be verified for the three input power levels in Fig. 7. The figures show n_e during the last period of the considered voltage source waveform.

For the three considered input power levels P_1, P_2 and P_3 the electron number density reaches a value of $1.5 \times 10^{19} m^{-3}$, $7.5 \times 10^{17} m^{-3}$ and $9.5 \times 10^{15} m^{-3}$ respectively. The obtained range for the electron number density is consistent with other works [33, 42].

It is well know that a larger electron number density leads to a more densely populated N_2 VDF [25] and, consequently, to higher reaction rates of reaction (9). Figures 8a, b and c report the calculated VDF at several time instants for the three considered input power densities. As it can be observed, the input power affects not only the relative populations of the vibrational states of N_2, but also the dynamics of the VDF evolution. In fact, for the lower considered input power density (P_3) the VDF starts to approach steady state for $t > 20$ms in Fig. 8c. Conversely, only 500μs are needed to reach a similar condition when the power is P_1 in Fig. 8a. A somewhat intermediate situation is yielded by P_1 in Fig. 8b. Moreover, comparing the typical plateau of the VDF shape in the three cases, one can notice that larger input power levels lead to an increase of the energy stored in vibrational excitation.

The latter quantity can be effectively described by the vibrational temperature, whose time behaviour during the three considered simulations is reported in Fig. 9a, b and c. For each plot two temperature profiles are provided, corresponding to the *two level* and the *all level* formulations in Eqs. (12) and (13), respectively.

We now focus on the differences yielded by the two calculation approaches. These figures show that these vibrational temperatures obtained by these two formulations are clearly different for longer times. This result is a consequence of the behavior of the tail of the VDF, which is not accounted for when using the two-level formulation.

Moreover, for the simulation performed at P_3 (Fig. 9c), the two values at the last considered time instant are nearly the same, i.e. $T_{v,first} \approx T_{v,All} = 2000$K. This means that the majority of the vibrational energy is stored in the first levels, populated by e-V collisions. Conversely, intermediate levels, which are usually populated through V-V collisions,

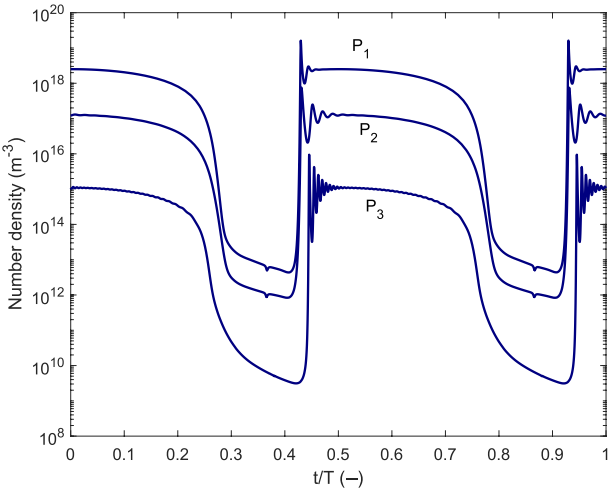

Fig. 7 Electrons number density during the last time period of the considered voltage source for all the levels of input power density.*T* indicates the period of the voltage source in each simulations

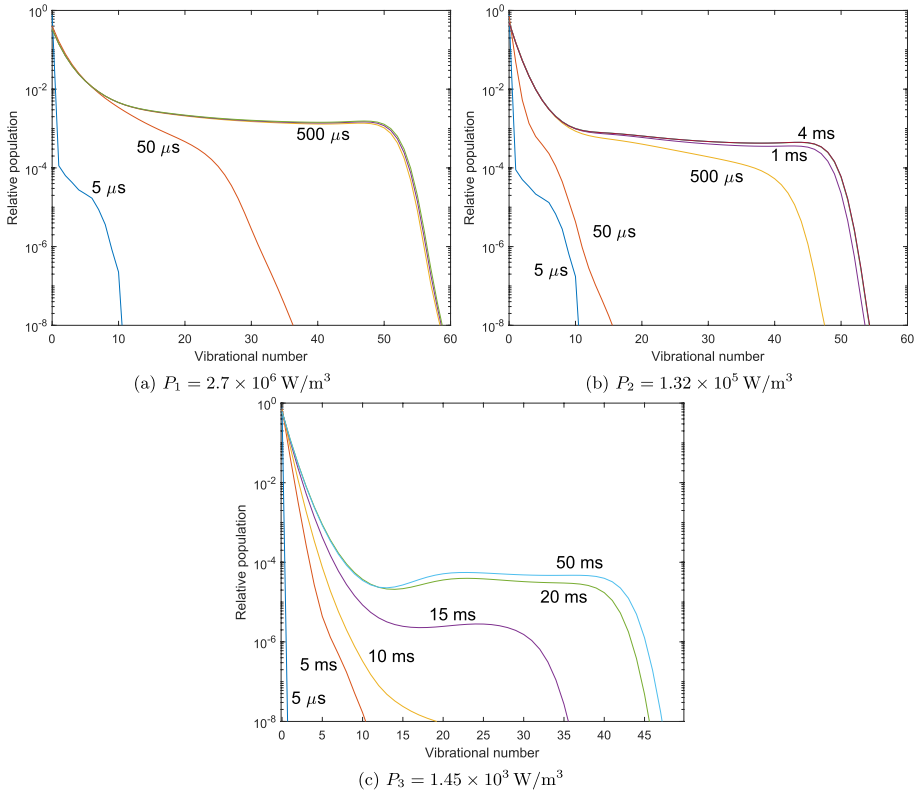

(a) $P_1 = 2.7 \times 10^6\,\mathrm{W/m^3}$ (b) $P_2 = 1.32 \times 10^5\,\mathrm{W/m^3}$

(c) $P_3 = 1.45 \times 10^3\,\mathrm{W/m^3}$

Fig. 8 Temporal evolution of N_2 VDF for the the input power densities considered in this work

remains almost empty. This phenomenon has been also observed in [43] for a pulsed DBD discharge in N_2. This fact is coherent with the previously discussed VDF plot in Fig. 8c at steady state, which reports a relative population of the intermediate vibrational levels below 10^{-4}.

Conversely, substantial differences of ~ 2000K and ~ 8000K are yielded by the two formulas for the two larger input power levels P_2 and P_1 in Fig. 8b and a, respectively. In this case, the VDF in Fig. 8b and a features a relative population of intermediate levels slightly below 10^{-3} and 10^{-2}, respectively. This indicates that the importance of V-V collisions grows with increasing power levels. Another interesting feature that can be noticed in the three figures is that the temperature oscillations increase with P. This can be explained by considering that with increasing power T_v is more and more determined by the population of higher levels. These are characterized by lower relaxation times with respect to lower levels, and hence are more subjected to the applied field oscillations.

NO_2

The input power influence has also been assessed focusing on NO_2 molecules, whose number density is strongly related to the ones of O_3 and NO. As shown in Fig. 6, the NO_2 number density follows the one of NO, which is one of the main precursor of this

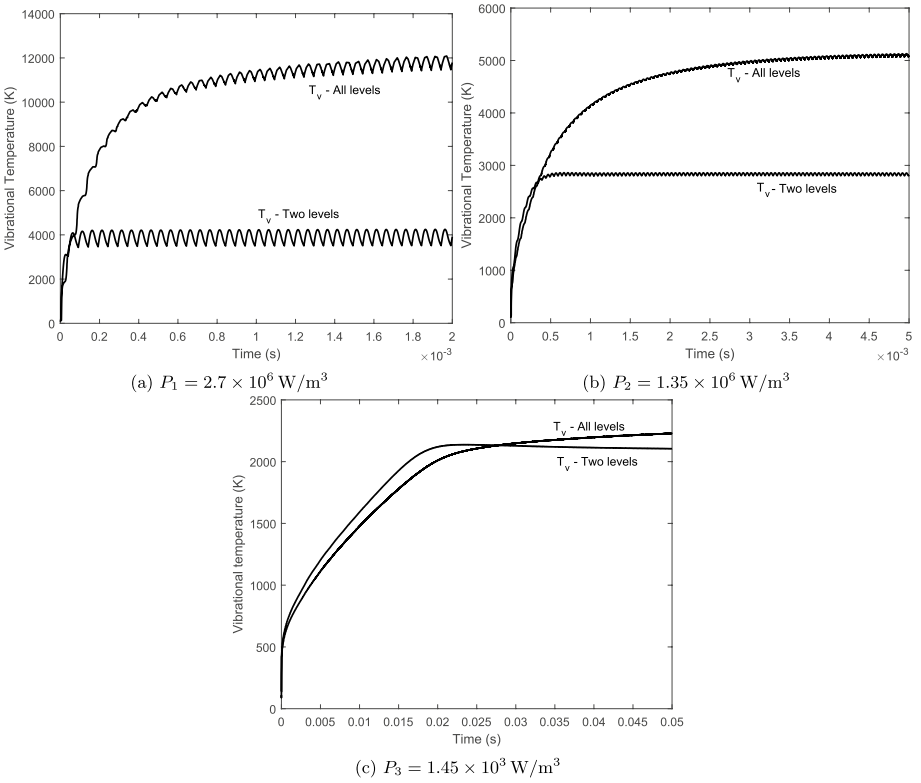

(a) $P_1 = 2.7 \times 10^6\ \mathrm{W/m^3}$ (b) $P_2 = 1.35 \times 10^6\ \mathrm{W/m^3}$

(c) $P_3 = 1.45 \times 10^3\ \mathrm{W/m^3}$

Fig. 9 N_2 vibrational temperature for three values of the considered input power level, obtained considering all the vibrational levels in Eq. (13) or just the first two according to Eq. (12)

species. In fact, ozone quenching by reaction (23) represents also one of the main formation channels for NO_2 molecules along with the other reaction (24) involving oxygen atoms:

$$NO + O(^3P) + N_2 \longrightarrow NO_2 + N_2. \tag{24}$$

The $O(^3P)$ behavior is reported in Figs. 10 during the last simulated period of the voltage source waveform. Its behavior during the entire simulations is reported in Figs. 6a, b, c.

Despite the $O(^3P)$ number density is depleted through reaction (9) by vibrationally-excited nitrogen molecules, whose number density increases with the input power, $O(^3P)$ raises for higher values of P. This is due to the fact that larger power levels lead to higher electron number densities, which activate reaction (20), $e + O_2 \longrightarrow e + O(^3P) + O(^3P)$, resulting in a larger $O(^3P)$ concentration.

The importance of reactions (23) and (24), whose rate constants are $k_{(23)} = 4.3 \cdot 10^{-18} \exp(-\frac{1560}{T})\mathrm{m^3/s}$ and $k_{(24)} = 1 \times 10^{-43}\mathrm{m^3/s}$, respectively, strongly depends on the considered input power level. In fact, for $P = P_3$ O_3 concentration is larger with respect to one of $O(^3P)$, and so does the reaction rate of reaction (23). Conversely, for P_2 and P_1, due to the already discussed ozone quenching mechanisms, the contribution to NO_2 formation through reaction (24) is more significant. These results are summarized in Table 3, and refer to the last considered half-period of the applied voltage waveform. Since

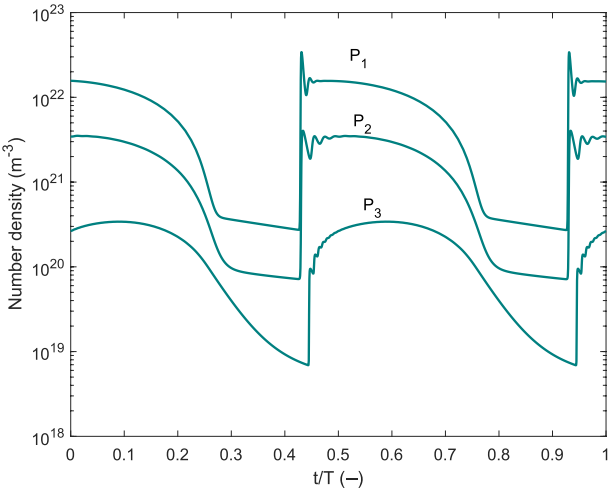

Fig. 10 $O(^3P)$ number density during the last time period of the voltage source for all the considered input power density levels. T indicates the time period in each simulations

Table 3 Reaction rates of reactions 23 and 24 dusing the last half-period of the applied voltage waveform for the considered input power levels and for two different $O(^3P)$ number densities

Reaction	P_1	P_2	P_3
(23)	$7.49\times10^{25}m^{-3}/s$	$5.08\times10^{25}m^{-3}/s$	$8.17\times10^{24}m^{-3}/s$
(24) (high $O(^3P)$)	$3.19\times10^{28}m^{-6}/s$	$9.26\times10^{26}m^{-6}/s$	$2.63\times10^{24}m^{-6}/s$
(24) (low $O(^3P)$)	$2.54\times10^{26}m^{-6}/s$	$1.64\times10^{25}m^{-6}/s$	$5.31\times10^{22}m^{-6}/s$

the $O(^3P)$ number density strongly varies during one half period, its highest and the lowest number density levels are reported.

Influence of the Zeldovich Mechanism

To conclude the analysis, three simulations have been performed without considering the Zeldovich mechanism to better understand the influence that this reaction has on the number densities of O_3, NO and NO_2 and its relation to the input power level. The time evolution of the three number densities is reported in Fig. 11, with and without the mechanism. This is repeated for the three values of the input power density. During the initial time instants of the simulations, the number densities of each species are approximately the same with and without the mechanism, because the vibrational levels $N_2(v > 12)$ are not populated yet. As soon as the number densities of intermediate vibrational levels start to increase (approximately at 0.05ms, 0.5ms and 25ms) reaction (9) begins to influence the discharge kinetics and the computed number densities with and without the Zeldovich mechanism start to differ. Table 4 reports the ratio between the number densities with and without reaction (9) for all the investigated input power levels, evaluated at the instants when the number densities percent difference is larger. These instants are highlighted in Fig. 11.

The greatest differences are obtained for the intermediate value P_2, even if the Zeldovich mechanism has a larger rate with the highest power P_1. This is because for larger power levels other reactions that are not relevant at lower input power become more important.

Table 4 Ratio corresponding to the maximum percent difference between the number densities with and without the Zeldovich mechanism.The instant at which these ratios are calculated are highlighted in Fig. 11

$n_{wZel}/n_{w/oZel}$	P_1	P_2	P_3
O_3	0.21	0.13	0.4
NO	10.7	36.5	7.38
NO_2	16.8	38.1	5.9

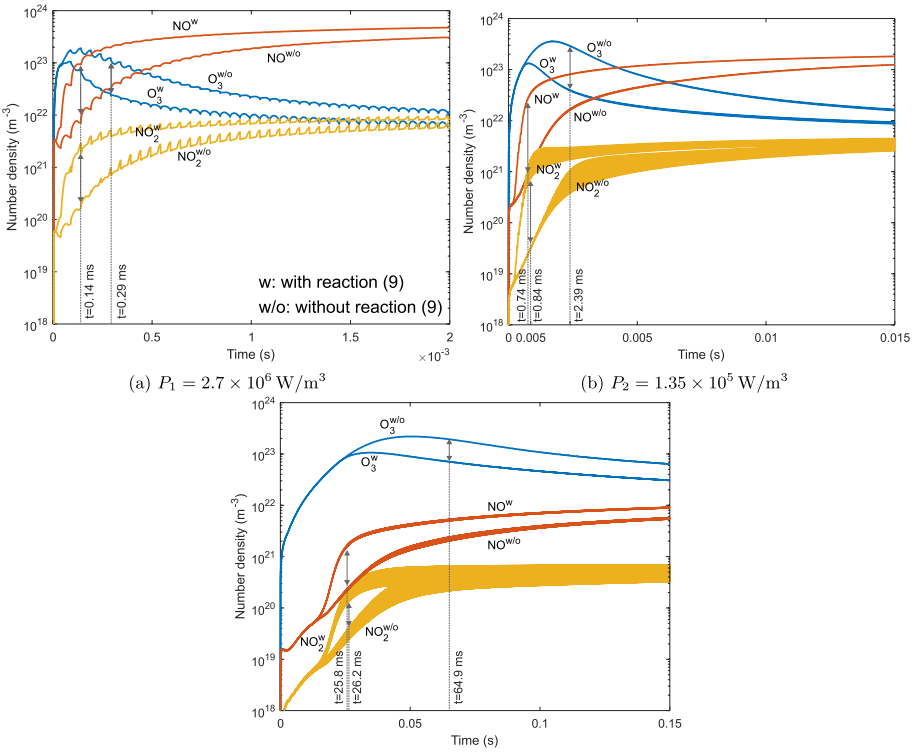

(a) $P_1 = 2.7 \times 10^6$ W/m^3 (b) $P_2 = 1.35 \times 10^5$ W/m^3

(c) $P_3 = 1.45 \times 10^3$ W/m^3

Fig. 11 Comparison between O_3, NO and NO_2 behavior for different levels of input power densities with and without reaction $N_2(v > 12) + O(^3P) \longrightarrow NO + N(^4S)$ (9). The arrows in figure and the corresponding time values indicate the instant at which the values of Table 4 are calculated

Regarding ozone consumption, reaction (25) plays an important role for large power due to the larger availability of electrons (see Fig. 7):

$$e + O_3 \longrightarrow e + O(^3P) + O_2. \tag{25}$$

For what concerns NO production, higher reaction rate comes from the process:

$$NO_2 + O(^3P) \longrightarrow NO + O_2. \tag{26}$$

In fact, the concentration of $O(^3P)$ and NO_2 increases with the input power, as reported in Fig. 10.

It is possible to conclude that, even is the reaction rate of the Zeldovich mechanism increases with the input power, its relative contribution is larger at intermediate power levels when reactions involving $O(^3P)$ and electrons are not preponderant yet.

Conclusions

In this study we developed a global model to study the chemical kinetics of a volumetric DBD reactor operating in humid air. The model incorporates a set of reactions in a ternary mixture of N_2, O_2 and H_2O coupled with an equivalent circuit model. We gave particular emphasis to the relation between vibrational excitation and some chemical species that are relevant for biological applications. First, a preliminary study has been carried out to assess the influence of humidity on the EEDF shape and to analyze the impact that the vibrational excitation of oxygen molecules has on the chemical kinetics of the discharge. We conclude that, under the conditions of this study, O_2 vibrational excitation does not play a significant role in the chemical kinetics of a DBD discharge at atmospheric pressure. Moreover, we found that humidity content influences the EEDF shape only for low reduced fields (< 20Td). Afterwards, we adopted the above mentioned kinetic model to evaluate the influence of N_2 vibrational excitation on the number density of O_3, NO_X, assessing the role of the Zeldovich mechanism $N_2(v > 12) + O(^3P) \longrightarrow NO + N(^4S)$. A series of simulations considering three different levels of input power density were performed, and the correspondent vibrational temperatures were calculated based on either the first two levels or all levels. The results show that the Zeldovich mechanism plays an important role on O_3 and NO_x chemical kinetics, and its influence is larger for intermediate power densities. In fact, for a low input power V-V collisions do not significantly populate the intermediate levels of the N_2 VDF (the ones that concur in NO formation). Conversely, at higher power levels the influence on O_3, NO and NO_2 of other processes that involve electrons and oxygen atoms becomes more significant. Future activities will include the experimental validation of the model, focusing on the measurements of the N_2 vibrational temperature and its evolution at different levels of input power density.

Author contribution All authors contributed to the study conception and design. A.P. wrote the original code, C.D.P. worked G.P, on the specific features of LoKI applied to the conditions of this work. G.P. prepared the first draft of the manuscript, carried on the simulations and performed the data collection and analysis. G.P. and A.P. prepared the figures. All authors commented on previous versions of the manuscript. A.C. and C.D.P. supervised the work. All authors read and approved the final manuscript.

Funding Open access funding provided by Alma Mater Studiorum - Università di Bologna within the CRUI-CARE Agreement. IPFN activities were supported by the Portuguese FCT, under projects UIDB/50010/2020 (https://doi.org/10.54499/UIDB/50010/2020), UIDP/50010/2020 (https://doi.org/10.54499/UIDP/50010/2020) and LA/P/0061/2020 (https://doi.org/10.54499/LA/P/0061/2020). The authors from the University of Bologna have received funding from the National Recovery and Resilience Plan (NRRP), Mission 04 Component 2 Investment 1.5 – NextGenerationEU, Project: Ecosister – Ecosystem for Sustainable Transition in Emilia-Romagna. Call for tender n. 3277 dated 30/12/2021 Award Number: 0001052 dated 23/06/2022.

References

1. Graves DB (2012) The emerging role of reactive oxygen and nitrogen species in redox biology and some implications for plasma applications to medicine and biology. J Phys D Appl Phys 45(26):263001
2. Puač N, Gherardi M, Shiratani M (2018) Plasma agriculture: a rapidly emerging field. Plasma Processes Polym 15(2):1700174
3. Dharini M, Jaspin S, Mahendran R (2023) Cold plasma reactive species: generation, properties, and interaction with food biomolecules. Food Chem 405:134746
4. Shimizu T, Sakiyama Y, Graves DB, Zimmermann JL, Morfill GE (2012) The dynamics of ozone generation and mode transition in air surface micro-discharge plasma at atmospheric pressure. New J Phys 14(10):103028
5. Pavlovich M, Ono T, Galleher C, Curtis B, Clark D, Machala Z, Graves D (2014) Air spark-like plasma source for antimicrobial NOX generation. J Phys D Appl Phys 47(50):505202
6. Graves DB (2017) Mechanisms of plasma medicine: coupling plasma physics, biochemistry, and biology. IEEE Transactions on radiation and plasma medical sciences 1(4):281–292
7. Seri P, Nici S, Cappelletti M, Scaltriti SG, Popoli A, Cristofolini A, Neretti G (2023) Validation of an indirect nonthermal plasma sterilization process for disposable medical devices packed in blisters and cartons. Plasma Processes and Polymers, p. e2300012
8. Bradu C, Kutasi K, Magureanu M, Puač N, Živković S (2020) Reactive nitrogen species in plasma-activated water: generation, chemistry and application in agriculture. J Phys D Appl Phys 53(22):223001
9. Attri P, Ishikawa K, Okumura T, Koga K, Shiratani M (2020) Plasma agriculture from laboratory to farm: a review. Processes 8(8):1002
10. Pierotti G, Piferi C, Popoli A, Cavedon M, Cristofolini A, Martines E, Riccardi C (2023) A novel two-stage kinetic model for surface DBD simulations in air. Plasma Sources Sci Technol 32(6):064005
11. Popoli A, Ragazzi F, Pierotti G, Neretti G, Cristofolini A (2023) A boltzmann electron drift diffusion model for atmospheric pressure non-thermal plasma simulations. Plasma 6(3):393–407
12. Colonna G, D'Ammando G, Pietanza L (2016) The role of molecular vibration in nanosecond repetitively pulsed discharges and in DBDS in hydrogen plasmas. Plasma Sources Sci Technol 25(5):054001
13. Sakiyama Y, Graves DB, Chang H-W, Shimizu T, Morfill GE (2012) Plasma chemistry model of surface microdischarge in humid air and dynamics of reactive neutral species. J Phys D Appl Phys 45(42):425201
14. Guerra V, Tejero-del Caz A, Pintassilgo CD, Alves LL (2019) Modelling n2–o2 plasmas: volume and surface kinetics. Plasma Sources Sci Technol 28(7):073001
15. Bourdon A, Vervisch P (2000) Analytical models for electron-vibration coupling in nitrogen plasma flows. J Thermophys Heat Transfer 14(4):489–495
16. Capitelli M, Ferreira CM, Gordiets BF, Osipov AI (2013) Plasma kinetics in atmospheric gases. Springer, Berlin
17. Pintassilgo CD (2012) Plasma chemistry in repetitively pulsed discharges in air at low pressures. Plasma Sources Sci Technol 21(3):035020
18. Tejero-del Caz A, Guerra V, Gonçalves D, Da Silva ML, Marques L, Pinhao N, Pintassilgo CD, Alves LL (2019) The Lisbon kinetics Boltzmann solver. Plasma Sources Sci Technol 28(4):043001
19. Tejero-del Caz A, Guerra V, Pinhão N, Pintassilgo CD, Alves LL (2021) On the quasi-stationary approach to solve the electron boltzmann equation in pulsed plasmas. Plasma Sources Sci Technol 30(6):065008
20. Budde M, Dias TC, Vialetto L, Pinhão N, Guerra V, Silva T (2022) Electron-neutral collision cross sections for h2o: I complete and consistent set. J Phys D Appl Phys 55(44):445205
21. Pitchford LC, Alves LL, Bartschat K, Biagi SF, Bordage M-C, Bray I, Brion CE, Brunger MJ, Campbell L, Chachereau A et al (2017) LXCat: An open-access, web-based platform for data needed for modeling low temperature plasmas. Plasma Processes Polym 14(1–2):1600098
22. Pancheshnyi S, Biagi S, Bordage M-C, Hagelaar G, Morgan W, Phelps A, Pitchford LC (2012) The LXCat project: Electron scattering cross sections and swarm parameters for low temperature plasma modeling. Chem Phys 398:148–153

23. Carbone E, Graef W, Hagelaar G, Boer D, Hopkins MM, Stephens JC, Yee BT, Pancheshnyi S, Van Dijk J, Pitchford L (2021) Data needs for modeling low-temperature non-equilibrium plasmas: the LXCat project, history, perspectives and a tutorial. Atoms 9(1):16
24. Alves LL, Coche P, Ridenti MA, Guerra V (2016) Electron scattering cross sections for the modelling of oxygen-containing plasmas. The European physical journal D 70:1–9
25. Loureiro J, Ferreira C (1986) Coupled electron energy and vibrational distribution functions in stationary N2 discharges. J Phys D Appl Phys 19(1):17
26. Alves LL, Marques L, Pintassilgo CD, Wattieaux G, Es-Sebbar E, Berndt J, Kovacević E, Carrasco N, Boufendi L, Cernogora G (2012) Capacitively coupled radio-frequency discharges in nitrogen at low pressures. Plasma Sources Sci Technol 21(4):045008
27. Guerra V, Loureiro J (1995) Non-equilibrium coupled kinetics in stationary N2–O2 discharges. J Phys D Appl Phys 28(9):1903
28. Armenise I, Esposito F (2021) N+ O2 (v) collisions: reactive, inelastic and dissociation rates for state-to-state vibrational kinetic models. Chem Phys 551:111325
29. Uddi M, Jiang N, Adamovich I, Lempert W (2009) Nitric oxide density measurements in air and air/fuel nanosecond pulse discharges by laser induced fluorescence. J Phys D Appl Phys 42(7):075205
30. Gordillo-Vázquez F, Donkó Z (2009) Electron energy distribution functions and transport coefficients relevant for air plasmas in the troposphere: impact of humidity and gas temperature. Plasma Sources Sci Technol 18(3):034021
31. Kozák T, Bogaerts A (2014) Splitting of CO2 by vibrational excitation in non-equilibrium plasmas: a reaction kinetics model. Plasma Sources Sci Technol 23(4):045004
32. Chirokov A, Gutsol A, Fridman A, Sieber K, Grace J, Robinson K (2004) Analysis of two-dimensional microdischarge distribution in dielectric-barrier discharges. Plasma Sources Sci Technol 13(4):623
33. Fridman A, Kennedy LA (2004) Plasma physics and engineering. CRC Press
34. Annušová A, Marinov D, Booth J-P, Sirse N, Da Silva ML, Lopez B, Guerra V (2018) Kinetics of highly vibrationally excited O2 (x) molecules in inductively-coupled oxygen plasmas. Plasma Sources Sci Technol 27(4):045006
35. Pietanza L, Colonna G, Capitelli M (2020) Extended plateaux in the vibrational and electron distribution functions of O2/O reacting plasmas in discharge and post-discharge conditions. Phys Plasmas 27(9):093510
36. Shkurenkov I, Adamovich IV (2016) Energy balance in nanosecond pulse discharges in nitrogen and air. Plasma Sources Sci Technol 25(1):015021
37. Lo A, Cessou A, Boubert P, Vervisch P (2014) Space and time analysis of the nanosecond scale discharges in atmospheric pressure air: I gas temperature and vibrational distribution function of n2 and o2. J Phys D Appl Phys 47(11):115201
38. Colonna G, Pintassilgo CD, Pegoraro F, Cristofolini A, Popoli A, Neretti G, Gicquel A, Duigou O, Bieber T, Hassouni K et al (2021) Theoretical and experimental aspects of non-equilibrium plasmas in different regimes: fundamentals and selected applications. The European Physical Journal D 75(6):1–35
39. MATLAB, *R2023b*. Natick, Massachusetts: The MathWorks Inc., 2023
40. Stefanovic I, Bibinov N, Deryugin A, Vinogradov I, Napartovich A, Wiesemann K (2001) Kinetics of ozone and nitric oxides in dielectric barrier discharges in O2/NOx and N2/O2/NOx mixtures. Plasma Sources Sci Technol 10(3):406
41. Brandenburg R (2017) Dielectric barrier discharges: progress on plasma sources and on the understanding of regimes and single filaments. Plasma Sources Sci Technol 26(5):053001
42. Neretti G, Taglioli M, Borghi CA (2018) Experimental determination and numerical evaluation under simplifying assumptions of the ozone concentration in an atmospheric-pressure air dbd plasma. The European Physical Journal D 72:1–9
43. Davies HL, Guerra V, van der Woude M, Gans T, O'Connell D, Gibson AR (2023) Vibrational kinetics in repetitively pulsed atmospheric pressure nitrogen discharges: average-power-dependent switching behaviour. Plasma Sources Sci Technol 32(1):014003